Journal of Raman Spectroscopy

WILEY

Journal of RAMAN SPECTROSCOPY

RESEARCH ARTICLE OPEN ACCESS

Beam-Generated Sample Evolution to Emphasize Spatial Inhomogeneities: The Example of HPO_4^{2-}-Containing Amorphous Calcium Phosphate

Sylvain Le Grill | Olivier Marsan | Christophe Drouet | Fabien Brouillet

CIRIMAT, Toulouse INP, Université Toulouse 3 Paul Sabatier, CNRS, Université de Toulouse, Toulouse, France

Correspondence: Sylvain Le Grill (sylvainlegrill@gmail.com)

Received: 3 April 2024 | **Revised:** 28 August 2024 | **Accepted:** 29 August 2024

Funding: The authors received no specific funding for this work.

Keywords: ACP | beam–matter interaction | cold sintering | multivariate analysis | Raman spectroscopy

ABSTRACT

Amorphous calcium phosphates (ACPs) represent a family of bioactive compounds particularly relevant to bone regeneration. However, due to their intrinsic metastability, their processing into 3D-shaped materials cannot be undergone by conventional sintering methods and requires cold sintering approaches. Also, their microstructure and local compositional changes still have to be explored in detail. To this aim, spectroscopy techniques are particularly appealing to probe local chemical environments at the microscale. Concerning ACPs, one question regards the distribution of (hydrogenated) phosphate species, as they may lead to various evolutionary trends. In this contribution, we purposely exploited the laser–beam interaction through Raman mapping to trigger the in situ HPO_4^{2-}-to-$P_2O_7^{4-}$ transformation. Analysis by a multivariate approach allowed us to spot $P_2O_7^{4-}$ clusters resulting from HPO_4^{2-}-rich initial domains. Moreover, a blue shift of the $\nu_1PO_4^{3-}$ band was noticed in the close vicinity of these clusters, thus evidencing a local evolution of the chemical composition of the ACP. These results, corroborated by differential thermal analysis, demonstrate the relevance of using the laser–sample interaction through local heating to probe the spatial evolution induced, in our case, by an ultrafast compaction process. Comparison of outcomes obtained using two different laser/power strategies finally evidenced the need to adapt the Raman analytical conditions to the behavior of the metastable material to analyze.

1 | Introduction

Raman microspectroscopy has proven to be a well-suited characterization technique to investigate the local repartition of species (i.e., through mapping) or local changes in chemical environments in diverse samples [1, 2]. It has thus been used for decades in a wide variety of application fields to take advantage of its versatility and relative ease of use, whether in dry or wet states. This opens up a large set of characterization opportunities and less feasible by other spectroscopy techniques such as solid-state nuclear magnetic resonance (NMR) or Fourier transform infrared (FTIR) (the latter being notably responsive to water).

One such field of interest is that of bone substitute materials, which includes in particular the family of calcium phosphates (CaP) [3–5], that can lead to the fabrication of bioactive bone substitutes capable of activating bone healing and potentially releasing active agents. Among appealing CaP compounds, amorphous calcium phosphates (ACPs) are often considered as precursors of new bone formation in vivo (prior to crystallizing into nanocrystalline nonstoichiometric apatite) and are growingly studied in this field [3, 6–8]. Besides their phospho-calcic nature close to natural bone mineral, their amorphous character enables a rather high resorption rate after implantation, thus allowing for rather rapid release of bioactive ions

(and possibly of associated drugs/bioactive molecules). One challenge remains, nonetheless, to prepare cohesive three-dimensional (3D) scaffolds of ACP while preserving its amorphous nature and potentially exhibiting a porous network to favor ion diffusion, resorption, and neovascularization.

Shaping ACP into such 3D constructs without inducing crystallization remains arduous. To face this difficulty, a new strategy has emerged in recent years, namely, by applying a "cold sintering" approach [9–12]. This strategy typically uses mechanical pressure to consolidate a powder without heating or under low-temperature heating, but exploiting non-thermally activated diffusion processes. The successful low-temperature shaping of ACP was shown to be effective by low-temperature spark plasma sintering ("SPS") (adding magnesium and carbonate ions as apatite growth inhibitors to stabilize the amorphous state) [13] or alternatively by ultra-high-pressure compaction [14, 15], eventually adding an external liquid phase to enhance the densification process [16].

Very recently [17], we presented and investigated the effect of ultrafast compression of an ACP phase at room temperature and under moderate pressure as another cold sintering approach. The peculiar ACP used in that study was obtained by spray drying (SD). This powder, with a Ca/P ratio of 1.3, contained a large amount of water (15.5 mol H_2O per mole) and HPO_4^{2-} ions (4 HPO_4^{2-} per 9 Ca^{2+}), notably higher than in regular Posner's clusters. This large amount of water in the initial powder was shown to enable this cold sintering strategy via ultrafast compression to be implemented successfully. 3D disk-like scaffolds were therefore produced, and they exhibited mechanical properties and porosity well suited for the production of bone scaffolds for non-loading zone and allowing appropriate handling/cutting for clinicians directly in a surgical room. That study also showed that, although the overall ACP composition did not undergo major alterations upon compression, a low amount of HPO_4^{2-} ions seemed to undergo changes in their local environment after compression. The relative stability of the overall chemistry of the powder with the applied pressure was expected as the use of a pressure usually witness change of structure (i.e., polymorphism) rather than change of chemistry [18–20]. Yet, the slight modifications pointed out by NMR and FTIR spectroscopies may be linked to the cold sintering strategy. Although the exact underlying mechanism is not fully elucidated, it is most probable that the water contained in the ACP composition should play an active role in the densification process even in such soft sintering conditions, as was already shown for other hydrated metastable compounds like biomimetic apatites and layered double hydroxides (LDHs) [11].

Although Raman (micro)spectroscopy is increasingly used in diverse fields of research including calcium phosphate–based bone substitutes, the scattering efficacy significantly depends on the nature of the species in presence, making it a rather "selective" technique. In fact, some species are particularly responsive, such as PO_4^{3-} or the pyrophosphate ion $P_2O_7^{4-}$. These ions actually provide deep information in terms of local environment modification and/or localization (for mapping) even at dilute concentrations. On the other hand, some species are only associated with a poor response, such as the hydrogenphosphate ion, HPO_4^{2-}. The latter will therefore provide only limited information in terms of evolution of the local environment or localization (for mapping) when they are poorly concentrated in the material of interest. In other words, an ortho/pyrophosphate composite can be mapped and distinguished more easily than an ortho/hydrogenphosphate composite [21].

In addition to this "pseudo" selectivity, Raman spectroscopy—as a laser-based technique—induces beam–matter interaction that may result in a local rise of temperature [22]. Depending on the analysis conditions, this increase of temperature can reach up to several hundreds of degrees Celsius, which may in turn induce locally alter the material studied and therefore change the Raman spectral signature. Although this effect is particularly desired and induced in the field of art and archaeological research [23, 24], it is generally sought to be a limitation in the field of biomaterials research, where the tendency is to prevent samples alterations upon beam exposure. However, the intentional recourse to such beam-induced amorphous-to-crystalline phase transformation thermal effects could be advantageously exploited to better reveal local heterogeneities of composition. In the field of CaP compounds, such an enhancement in terms of "chemical mapping" could potentially be expected for HPO_4^{2-}-bearing phases, as these hydrogenphosphate ions will condense into pyrophosphate ions $P_2O_7^{4-}$ beyond a certain temperature threshold (typically in the range 300–450°C for HPO_4^{2-}-containing ACP or biomimetic apatite, based on thermal analyses), following Equation (1). By inducing the local formation of such pyrophosphate ions ($P_2O_7^{4-}$), the localization of the HPO_4^{2-} present prior to the condensation reaction can be deduced.

$$2\,HPO_4^{2-} \rightarrow P_2O_7^{4-} + H_2O \quad (1)$$

This approach has been pursued in the present work, as an illustrative example of the exploitation of beam–sample interaction, for the analysis of ACP discs consolidated by ultrafast compression in a previous study [17], with the view to further investigate the spatial distribution of species after this "cold sintering" process, and thus better understand the possible mechanisms at play. To this aim, Raman microspectroscopy mapping exploiting this beam–matter interaction was implemented and completed by differential thermal analysis (DTA). To our knowledge, no publication refers to the use of the beam–matter interaction to induce a chemical reaction in situ to create highly sensitive species from less sensitive ones, with the view to facilitate the spatial distinction of chemical species.

2 | Materiel and Methods

2.1 | Reagents

Phosphoric acid, PA (H_3PO_4 85%), and monohydrate calcium acetate, CA ($Ca(CH_3COO)_2$, H_2O) were purchased from Sigma-Aldrich (Darmstadt, Germany).

2.2 | Powder Synthesis and Cold Sintering Pellet Fabrication

The HPO_4^{2-}-bearing ACP powder used in this work was obtained according to our previous study [25]. Briefly, a calcium

phosphate solution was prepared by dissolving 5 g of CA in 1 L of deionized water and with the addition of 1.18 mL of PA. The addition of PA was done under vigorous stirring dropwise in a minute of time. When the clear transparent solution is ready, it is spray-dried using a BUCHI B 290 mini spray drier (Büchi Labortechnik AG, Flawil, Switzerland) with an inlet temperature of 160°C, a gas flow of 414 $L.h^{-1}$, and a liquid flow of 0.3 $L.h^{-1}$.

A white powder was obtained after spray drying, composed of grains of about 3 μm in size, themselves exhibiting a substructure of aggregated nanoparticles of around 100 nm. The powder obtained was stored at room temperature in a closed vial without any further treatment.

To prepare the ACP pellet, this powder was processed using a pharmaceutical-grade compaction simulator STYL'One Evolution (Medelpharm, Beynost, France) with a EuroB flat-faced punches (6 mm) at different forces ranging from 25 to 200 MPa at 100% speed and with a dwell time of 20 ms. The details of the cold sintering process and results are given in our previous article [17].

2.3 | Raman Mapping

Raman analyses of the pellet were performed using a confocal RAMAN LabRAM Evolution Horiba Yvon Jobin microscope. The samples were exposed to continuous laser radiation supplied by a diode laser at 532 nm with a power of 48.6 mW. These analysis conditions were selected to trigger the condensation of the HPO_4^{2-} ions into $P_2O_7^{4-}$ under the beam, with the aim to avoid stronger structural alterations leading to ACP crystallization.

For these mapping experiments, the samples were placed under an Olympus BX 41 microscope and focused under an objective 100× numerical aperture of 0.90, which gave the system a lateral resolution of 0.72 μm (1.22 × λ / ON) and an axial resolution of 2.61 μm (4 × λ/O.N2). The maps were acquired using an XYZ motorized stage with a measurement step of 5 μm along the X and Y axes. The use of an autofocus, whose amplitude range was optimized with the roughness of the area studied, allowed for the self-adjustment of the focus. The representation of the Raman mapping pixel corresponds to the main contributor spectra, and RGB unmixed mode representation was preferred to facilitated the reading.

A reference Raman mapping was also achieved in non-altering conditions using a 633 nm laser with a power of 4.24 mW and the same objective as above.

The equipment was wavenumber-calibrated with a silicon standard using the first-order line of silicon at 520.7 cm^{-1}, with an accuracy of ± 1 cm^{-1}.

a. The spectrum of each point was acquired using a 600 tr. mm^{-1} grating with a spectral resolution of 1 cm^{-1} and collected with a quantum well detector cooled to −60°C by double Peltier effect (CCD Synapse). Each spectrum of the maps was acquired with a 10 s time and 1 accumulation. Data processing was performed using the LabSpec 6 software (Version 6.6.1.11). Multivariate analysis (MVA) was performed using multicurve regression (MCR) of the MVA module of the LabSpec 6 software. A multivariate curve resolution alternating least squares (MCR-ALS) algorithm was implemented to identify complex mixture constituents and contributions [26]. Two requirements are only needed to apply MCR to a multicomponent system, namely, the experimental data can be structured as a two-way data matrix or a multiset structure

b. The data set can be explained reasonably well by a bilinear model using a limited number of components.

The MCR bilinear model is usually written $D = CS^T$ where D is the raw data set, for example, a spectroscopic data table, and S^T and C are the matrices of the pure spectra and the related concentration profiles for each of the compounds (contributions), respectively.

The number of variables (number of components) was set in order to adjust the cumulative variance of the components as close of 100% as possible.

All spectra were recorded at ambient temperature and pressure.

2.4 | DTA

The powder and consolidated pellets obtained upon mechanical pressure at 25 and 200 MPa were characterized using a SETARAM (Setsys Evolution System, France) TGA/DTA apparatus, from 25°C to 1000°C at 5°C/min under air flow (20 mL/min), preceded by a plateau at 25°C for 30 min for preliminary equilibration.

3 | Results and Discussion

In order to better resolve the position of the HPO_4^{2-}-bearing compounds within the ACP pellet obtained by ultrafast compression, a Raman mapping strategy was set up. A typical approach was to use the 532 nm laser beam with the objective to transform locally the low responsive HPO_4^{2-} ions into high responsive $P_2O_7^{4-}$ species. To identify and point out the possible changes of chemical environment and/or the spatial distribution of the different phosphate groups induced by the compaction process, a mapping of a radial section of the 100 MPa pellet was performed.

In a first-intention stage, a univariate analysis approach was used to interpret the data. Results are shown in Figure 1a and the associated spectra are specified in Figure 1b. This analysis suggests the presence of three different components, as emphasized in Figure 1ai–iii by the spatial distribution represented as split channels with three mapping colors. The red color is associated with a low signal, likely attributable to the Raman spectrum noise. It may be noted that the spectral signature of magnesium stearate (MgSte)—used as lubricant during the compression process—cannot be detected here, which can be associated with the low amount of MgSte used or the possible degradation (burn) of

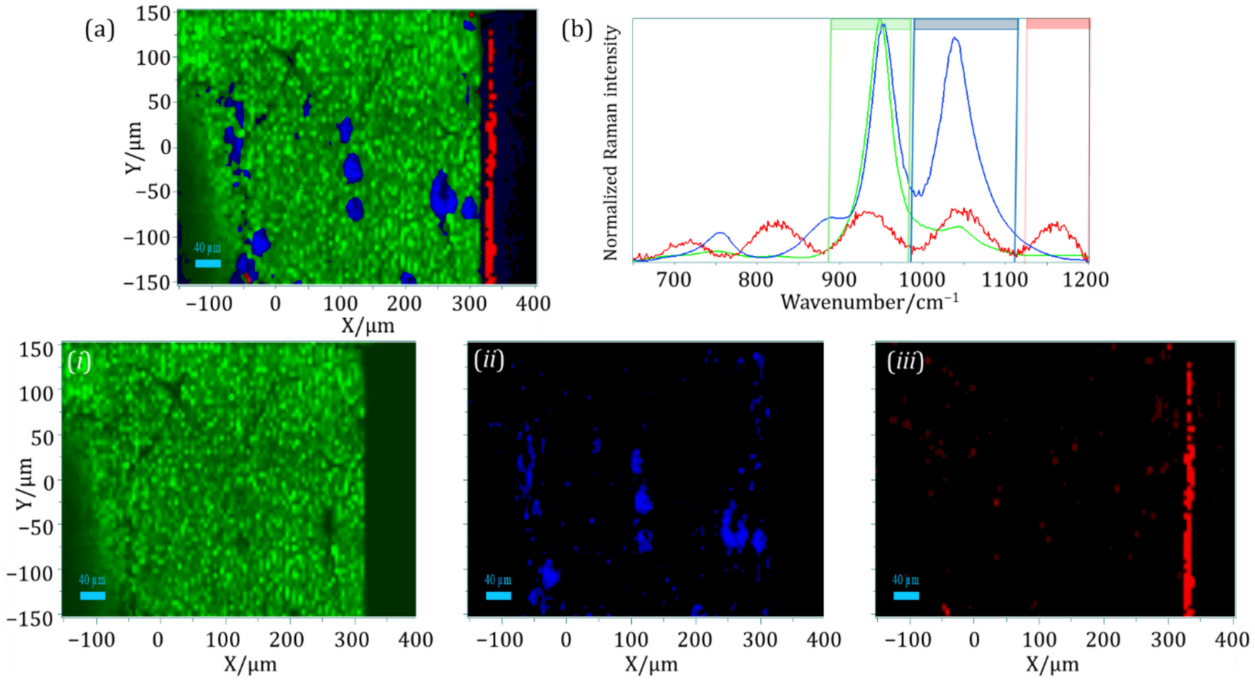

FIGURE 1 | Monovariate analysis of Raman mapping (532 nm, 48.6 mW) of a radial section of a 100 MPa consolidated ACP pellet. (a) Raman mapping of the split channel (i), (ii), and (iii) and the corresponding spectra (b).

this component. Two other spectral contributions are observed via this univariate data analysis: a major one, in green that corresponds to the band area integration around 950 cm^{-1} and that can be associated with the ν_1PO_4 vibration mode of the PO_4^{3-} ions in ACP [27], and a minor one, in blue that corresponds to the area integration of the 954 and 1048 cm^{-1} bands. The blue contribution is characterized by three main bands at 954 (main), 1048 (medium), and 750 cm^{-1} (low). Whereas the band at 954 cm^{-1} relates to $\nu_1PO_4^{3-}$ with a modified environment compared to regular ACP, the two other bands are assignable to $P_2O_7^{4-}$ ions (respectively corresponding to the ν_sPO_3 and $\nu_{as}POP$ vibration modes) [28]. These two latter peaks (at 1048 and 750 cm^{-1}) were not present in the initial powder before compression, neither in the Raman spectra recorded in our previous study using a less powerful red laser (633 nm at 1 mW). They may thus reasonably be considered as the result of the condensation of HPO_4^{2-} ions into $P_2O_7^{4-}$ ions. The relative abundance of the three colors corresponds to 78.7% of green, 15% of blue, and 6.3% of red (data extract from LabSpec6 software): The large number of green pixels (i.e., relatively unchanged ACP) is in agreement with the statement in our previous paper that the overall composition of the ACP after ultrafast compaction stays essentially unchanged except for some HPO_4^{2-}. These results suggest that our enhancing strategy based on beam–matter interaction has successfully allowed Equation (1) to occur, thus facilitating the localization of initial HPO_4^{2-} ions in the examined sample.

However, because of the rough univariate analysis approach implemented to obtain Figure 1, it is not clear if the bands occurring within the blue component are due to a physical mixture of (modified) ACP and calcium pyrophosphate or a solid solution (viz., modified ACP phase incorporating some $P_2O_7^{4-}$ ions). To overcome the limitation regarding the identification of the blue contribution in Figure 1, a more developed data interpretation strategy using a MCR has been implemented. This chemometric approach may indeed allow identifying "hidden" information for complex data sets and could therefore prove helpful for a better identification of species. The resulting Raman mapping is given in Figure 2a, and the associated spectra are reported in Figure 2b, the former showing a general good correspondence with the univariate analysis. However, a decomposition into four main components (as opposed to 3 in the univariate approach) appears more suitable. Components #1 at 950 cm^{-1} (in green) and #3 at 954 cm^{-1} (in purple) can be attributed to the orthophosphate phase (ACP), the latter being thus blue-shifted compared to the former, and characterized by a narrower width. Component #4 (in blue) corresponds to the pyrophosphate signature at 1048 and 750 cm^{-1}. Finally, component #2 (in red) corresponds to the Raman spectrum background (noise).

The presence of clearly split spectra allows us to assess that the sample is mainly a physical mixture of (modified) ACP and calcium pyrophosphate after the beam–matter interaction (Figure 2b). However, spectra #3 and #4 present a minor band at 1048 and 954 cm^{-1}, respectively, suggesting also a partial incorporation of pyrophosphates in the orthophosphate phase and vice versa. This partial blending of the two phases can be interpreted as a progressive continuous domain between the different areas (interphase) rather than an abrupt crossing from one phase to the other.

To further investigate the spatial proximity of the identified phases, Figure 2c,d was plotted. On these plots, a pixel is represented by a point for which the coordinates characterize the contribution of the different component. A pixel with the equivalent amount of two components will be close to the bisecting line (represented by red dots); and the farther the point is from this

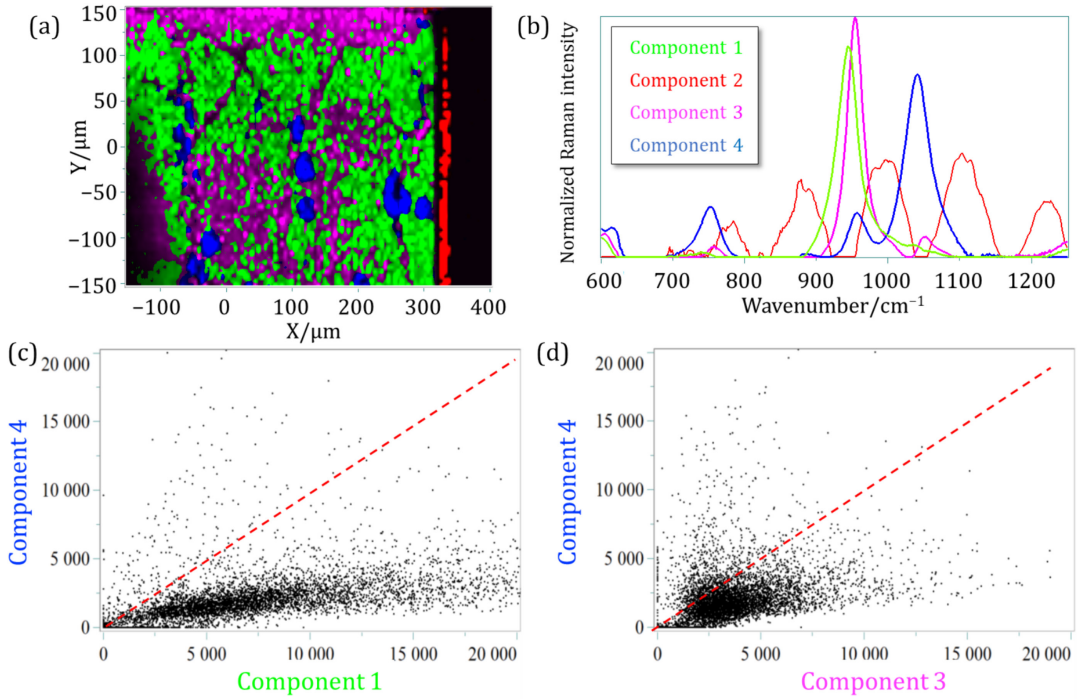

FIGURE 2 | Multivariate analysis of Raman mapping (a) of the section of an ACP pellet consolidated at 100 MPa, associated spectra (b), contribution of component 4 and component 1 (c), and component 4 and component 3 (d) per pixel.

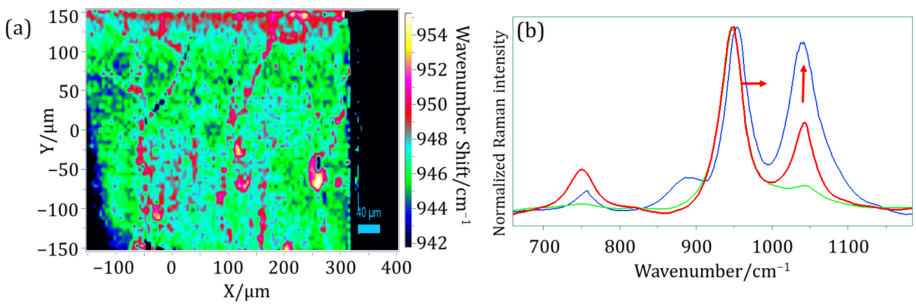

FIGURE 3 | (a) Raman mapping of the 950 cm^{-1} $\nu_1PO_4^{3-}$ band shift and (b) superimposition of three spectra to emphasize the relationship between the 950 cm-1 blue shift and the intensity of the 1048 cm^{-1} band of $P_2O_7^{4-}$ ions.

line, the less components are in equivalent proportion. Figure 2c thus presents this analysis with components #4 and #1 (i.e., pyrophosphate and the unchanged ACP). As may be seen, the overall cloud of points is far from the bisecting line and close to the abscissa axis (the non-modified ACP), indicating that components #4 and #1 are rather distinct from each other. On the other hand, Figure 2d shows a higher concentration of points in the close vicinity of the bisecting line. This depicts a close proximity between component #4 (pyrophosphate) and component #3 (modified or blue-shifted ACP). In turn, this result indicates that the formation of the pyrophosphate-rich phase and the modified ACP are spatially close.

Additional information may be drawn from the exploration of the blue shift of the 950 cm^{-1} $\nu_1PO_4^{3-}$ band. Figure 3a represents the corresponding mapping. It can be observed that the more $P_2O_7^{4-}$ phase is present and densely packed, the more shifted the 950 cm^{-1} band is. These two phenomena seem therefore concomitant. Figure S1 presents a superimposition of the Raman mapping from Figure 1aii and Figure 3a. It emphasizes the spatial coexistence of the 1048 cm^{-1} band and the 950 cm^{-1} blue shift. Figure 3b also illustrates this effect, with a greater blue shift when increasing the intensity of the band at 1048 cm^{-1} relating to pyrophosphate (component #4). This result indicates a change in the local environment of the PO_4^{3-} ions in the surrounding of the $P_2O_7^{4-}$-rich domains or "clusters." A positioning of the $\nu_1PO_4^{3-}$ band at higher Raman shift could correspond to an evolution from an amorphous environment of PO_4^{3-} ions to a more OCP-like environment. In fact, the $\nu_1PO_4^{3-}$ Raman bands of the OCP phase are located at 959 and 966 cm^{-1} [27]. The overall formula of the starting ACP powder used in this study [17] is $[Ca_3(PO_4)_2]_2.[CaHPO_4]_3$. 15.5 H_2O (corresponding to a particular Ca/P molar ratio of 1.3). Interestingly, this composition can be rewritten in the form $[Ca_8(PO_4)_4(HPO_4)_2]$, $[CaHPO_4]$, 15.5 H_2O, then evidencing some OCP-like and DCPD-like subcomponents (both rich in HPO_4^{2-} ions). The compaction of this ACP powder might thus have induced a modification in the organization of the ions or clusters of ions while not totally demixing into separate OCP and DCPD phases.

If we admit that $P_2O_7^{4-}$ ions result from the condensation of neighboring HPO_4^{2-}, the pyrophosphate-rich domains can be the signature of inhomogeneities of the HPO_4^{2-} dispersion in the sample prior to the condensation reaction (1). In fact, in the previous study [17], we demonstrated that few components of the hydrated layer were impacted with the applied pressure. Among them, some HPO_4^{2-} ions were nonetheless found to undergo a change in their local environment. These changes can be associated with the clustering of HPO_4^{2-} ions that is here highlighted by the Raman mapping and the observation of $P_2O_7^{4-}$ clusters. In fact, one of the underlying mechanisms of consolidation with the cold sintering approach relies on the mobility of the ions constituting the hydrated layer. By bringing together two adjacent hydrated layers (from neighboring particles), their ionic components can interact/bind and therefore induce the consolidation of the material, as was suggested before for biomimetic apatites [11]. However, the mobility of the hydrated layer ions is probably not limited solely to the surrounding hydrated layers but may also affect a larger volume within the consolidated pellet. This may be facilitated by the transient formation of a liquid (or liquid-like) phase during the cold sintering process. Beside such ion diffusion phenomena, water itself is also likely affected by the consolidation process, and several cold sintering studies have indeed reported the loss of structural water upon consolidation. In the present case, about 25 wt% of water was found to be removed from the material upon our ultrafast compaction process. All of this implies that diffusive mechanisms are at play and likely affect all components (ions and water) of the amorphous compound. By diffusing, the water can carry ions that can further lead to a distribution of ion clusters. The stability of $Ca^{2+} \bullet HPO_4^{2-}$ ion pairs has been established in solution [29–31]. However, within the ACP pellet, such ion pairs may present a different stability and potentially clusterize, which could explain our present observations from Raman mapping. This clusterization tendency might also remind the "amorphous calcium hydrogenphosphate phase" (ACHP) referred to by Eden et al., although this was not involving a cold sintering setting. The spatial partitioning of the HPO_4^{2-} and the PO_4^{3-} phases therefore creates HPO_4^{2-}-rich domains surrounded by OCP-like PO_4^{3-} in an overall matrix of essentially unchanged ACP. The overall mechanisms involved in the compaction of ACP and with the laser interaction are summarized in Figure 4.

The HPO_4^{2-} clustering combined with the beam–matter interaction and the associated temperature rise offer a propitious environment for condensation reaction (1) to occur. This normally happens at relatively high temperature (e.g., in the range of 350–600°C [32]); however, the beam–matter interaction could cause a local temperature rise sufficient to trigger this reaction.

All of the above Raman analyses were carried out with a diode 532 nm laser at a power of 48.6 mW (on the pellet compacted under 100 MPa), as the main objective was to exploit the beam/material interaction to finely trigger the local HPO_4^{2-}-to-$P_2O_7^{4-}$ condensation reaction; and our above results confirmed the success of this approach to analyze metastable compounds such as ACPs. It is a necessary step to evaluate, on the one hand, the presence and value of a potential laser power threshold for this condensation and, on the other hand, the effect of the accumulation of energy caused by the mapping mode. Figure S2 shows Raman analysis obtained on spots and carried out with different laser wavelengths and powers. Key results are that the $\nu_s PO_3$ band at 990 cm^{-1}, the ν_2 P-OH elongation band, and both deformation bands giving rise to components at ~1072, ~910, ~535, and ~390 cm^{-1}, respectively [33], characteristic of a hydrogenphosphate-bearing phase, decrease in intensity when the laser power reaches a value of 12.15 mW (25% of the maximum 532 nm laser output) and above. This decrease is associated with the increase of $\nu_s PO_3$ band intensity at 1048 cm^{-1} but also at $\nu_s POP$ at 762 cm^{-1} characteristic of the pyrophosphate phase [28], attesting to the HPO_4-to-P_2O_7 condensation reaction. These observations suggest that the "condensation threshold" is in the 12–24 mW power range. However, the more intense the laser power, the easier the identification of the bands due to a higher intensity of the ν_S PO_3 pyrophosphate band as it can be observed on the 532 nm laser at 100% maximum output (48.6 mW). Moreover, the resulting Raman mapping and relating monovariate analysis outcomes with a 633 nm laser at 4.24 mW (100% of the maximum 633 nm laser output) are represented in Figure 5a for the same 100 MPa sample as previously. In this figure, we can observe a relatively homogeneous distribution of the green (950 cm^{-1} relating to PO_4^{3-} in ACP) and blue (992 cm^{-1} possibly relating to HPO_4^{2-} in ACP) colors and with a similar overall Raman signature to the starting powder. Also, no specific blue shift of the 950 cm^{-1} band can be detected. And

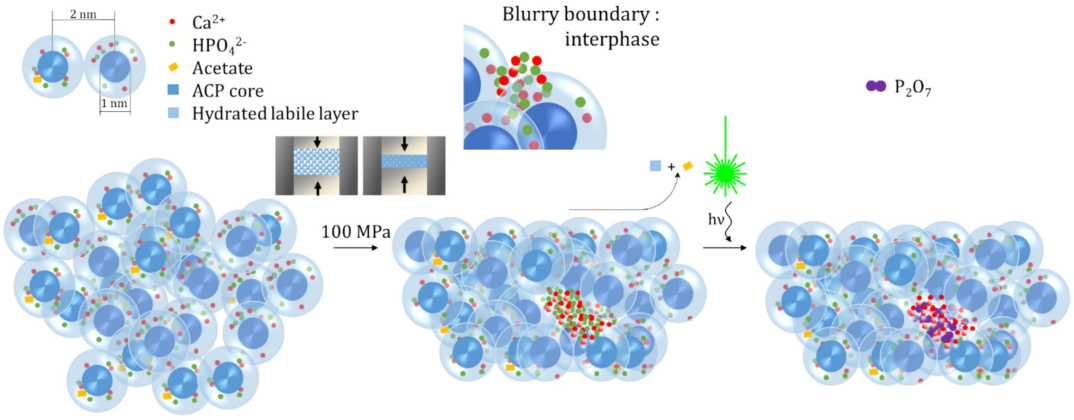

FIGURE 4 | Schematic representation of the mechanisms involved in the successive steps upon ACP compaction and Raman analyses. From left to right, the initial powder is homogeneous with a hydrated layer that embeds mobile ions. The compaction then affects the mobility of species within the hydrated layer and triggers the clustering of "$Ca^{2+} \bullet HPO_4^{2}$" ion pairs. Interaction with the laser finally triggers the condensation of HPO_4^{2-} ions into $P_2O_7^{4-}$ allowing Raman mapping of $P_2O_7^{4-}$-rich clusters and thus revealing the localization of initially HPO_4^{2-}-rich domains.

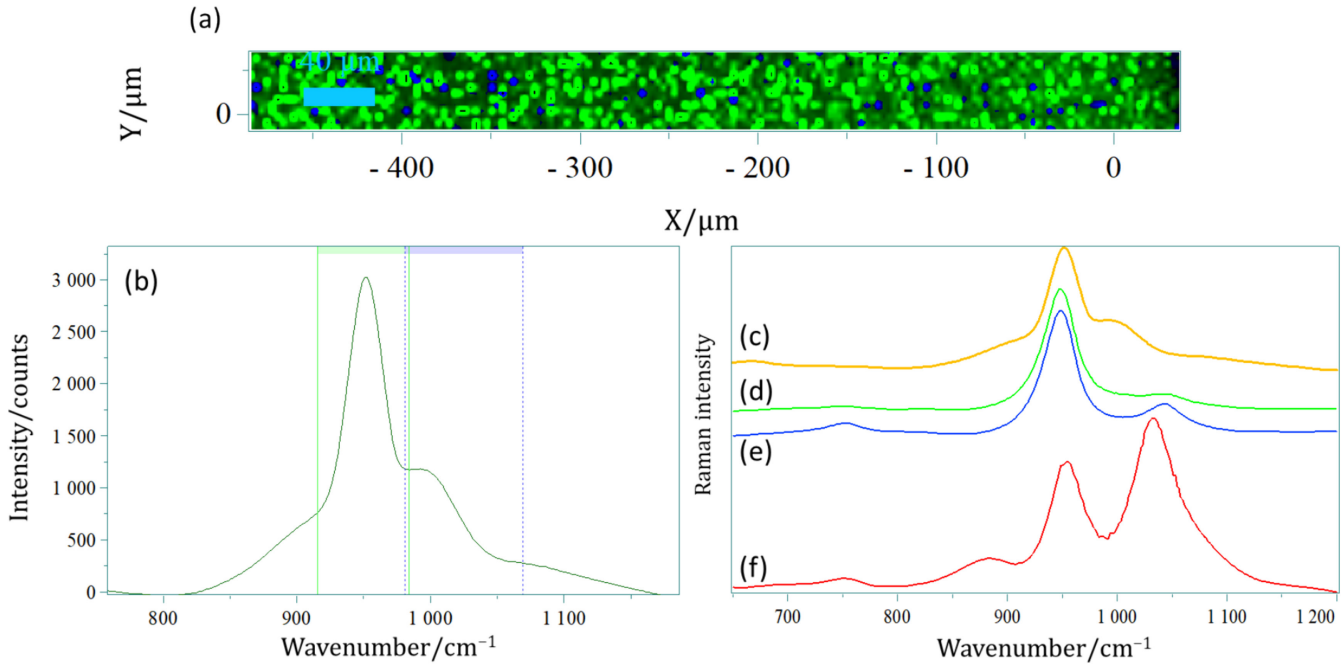

FIGURE 5 | (a) Monovariate Raman mapping recorded with a He–Ne 633 nm laser and (b) associated Raman spectra to identify the two associated green and blue components and comparison of (c) average spectrum of the 633 nm, (d) average spectrum of the 532 nm of the green area of Figure 2, (e) average spectrum of the 532 nm of the purple area of Figure 2, and (f) average spectrum of the 532 nm of the blue area.

most importantly, the beam–sample interaction using the less powerful 633 nm laser did not lead to a detectable contribution at 1048 cm^{-1}, thus insinuating the absence of pyrophosphate formation. These last analyses therefore show that these less energetic conditions are not adequate to deeply probe the modification of the HPO_4^{2-} ions environments in calcium phosphate phases, although beam–matter interaction by Raman analysis using the more powerful 532 nm laser appears particularly suitable to this aim.

DTA from 25°C to 1000°C at a 5 $K.min^{-1}$ rate were conducted in air on the starting powder and on pellets corresponding to increasing pressures of compaction. A focus on the exothermic peak at 700°C is provided in Figure S3 (it may be noted that no further significant exothermic peak could be detected in the range of 600–1000°C; Figure S3, top right insert). On the initial powder, only one broad exothermic peak is detected in the DTA plot. However, analysis by Raman spectroscopy of the sample heated to 1000°C demonstrated that two crystallized phases are present and identified as β-TCP and β-CPP in accordance to our previous study [17]. This suggests that several crystallization phenomena concurred to contribute to this exothermic event. A modification of this exothermic peak aspect is clearly seen after compaction, with a general tendency to occur as lower temperature and with the presence of two maxima. A closer analysis toward the lower temperature portion of the DTA signal further allows identifying a third underlying and broad contribution. The mathematical decomposition of the DTA curve in this temperature region was undergone using three Gaussian components. The illustrative example of the sample compacted at 25 MPa was added in Figure S3 (the curve of the mathematical fit has been downshifted for the sake of clarity). Among these three components, the curves corresponding to "gauss 1" and "gauss 2" are rather sharp exothermic contributions, whereas "gauss 3" is very broad. Although the two former contributions can likely be attributed to separated crystallization peaks for the β-TCP and β-CPP phases cited above (also evidenced by Raman spectroscopy on the pellets), it is reasonable to suggest that the broad contribution could be related to unseparated β-TCP/β-CPP phases crystallizing from the unchanged ACP. The corresponding areas under these three Gaussian components was evaluated and reported in Table S1 for pellets prepared at 25 and 200 MPa. These results point out an increase of the area under the two narrow peaks with the compaction. On the basis of our discussion based on Raman mapping in the previous paragraphs, the clearer detection of these two sharp peaks could then be explained by the formation of clusters or seeds of either PO_4^{3-}-rich or HPO_4^{2-}-rich domains, easing the crystallization of β-TCP and β-CPP, respectively.

4 | Conclusion

ACPs are particularly appealing bio-inspired compounds in the field of regenerative medicine as in orthopedics and maxillofacial surgeries. However, a series of ACPs can be prepared by diverse wet chemistry approaches, ending up in a wide family of amorphous compounds with various possible ionic compositions and water contents. In turn, these different compositions likely modify noticeably the thermodynamic stability and the reactivity of these ACP compounds, making them particularly relevant as tunable bone substitutes. The processing of ACPs is however made difficult due to their metastability, and cold sintering strategies have been developed, including by ultrafast powder compaction. One question however systematically remains on the possible presence of compositional inhomogeneities and the potential segregation of ions prone to evolve upon compaction or further processing into separate phases. In the

present contribution, we have exploited, in an original way, the laser beam–matter interaction through in-depth Raman mapping analyses to purposely induce in situ controlled evolution of ACP pellets and thoroughly monitor vibrational features. With the objective to determine the localization of HPO_4^{2-}-rich domains within the compacted samples, we have thus exploited the local rise of temperature produced by the laser to force the HPO_4^{2-}-to-$P_2O_7^{4-}$ local transformation. Raman mapping, associated with mono- and multivariate analyses and corroborated by DTA experiments, allowed us to show the local formation—upon laser irradiation—of HPO_4^{2-}-rich clusters within the samples, thus complementing our previous investigations. This approach based on beam–sample interaction, often considered as a drawback of the Raman technique, was here advantageously implemented, provided that the laser characteristics (here 532 nm, 48 mW) are adapted to the metastable behavior of the material of interest.

Acknowledgments

The authors extend their gratitude to the I2M laboratory (Bordeaux, France) for assistance with pellet manufacturing, especially V.M. and P.T. The corresponding author would also like to thank R.G., C.B., and P.G. for valuable and meaningful discussions.

References

1. P. Rostron and D. Gerber, "Raman Spectroscopy, a Review," *International Journal of Engineering and Technical Research* 6 (2016): 50–64.

2. S. Wachsmann-Hogiu, T. Weeks, and T. Huser, "Chemical Analysis In Vivo and In Vitro by Raman Spectroscopy—From Single Cells to Humans," *Current Opinion in Biotechnology* 20 (2009): 63–73.

3. J. Mahamid, A. Sharir, L. Addadi, and S. Weiner, "Amorphous Calcium Phosphate Is a Major Component of the Forming Fin Bones of Zebrafish: Indications for an Amorphous Precursor Phase," *Proceedings of the National Academy of Sciences of the United States of America* 105 (2008): 12748–12753.

4. N. J. Crane, V. Popescu, M. D. Morris, P. Steenhuis, and M. A. Ignelzi, "Raman Spectroscopic Evidence for Octacalcium Phosphate and Other Transient Mineral Species Deposited During Intramembranous Mineralization," *Bone* 39 (2006): 434–442.

5. J. A. Stammeier, B. Purgstaller, D. Hippler, V. Mavromatis, and M. Dietzel, "In-Situ Raman Spectroscopy of Amorphous Calcium Phosphate to Crystalline Hydroxyapatite Transformation," *MethodsX* 5 (2018): 1241–1250.

6. I. Roohani, S. Cheong, and A. Wang, "How to Build a Bone? – Hydroxyapatite or Posner's Clusters as Bone Minerals," *Open Ceramics* 6 (2021): 100092.

7. S. Von Euw, W. Ajili, T. H. C. Chan-Chang, et al., "Amorphous Surface Layer Versus Transient Amorphous Precursor Phase in Bone – A Case Study Investigated by Solid-State NMR Spectroscopy," *Acta Biomaterialia* 59 (2017): 351–360.

8. K. He, M. Sawczyk, C. Liu, et al., "Revealing Nanoscale Mineralization Pathways of Hydroxyapatite Using In Situ Liquid Cell Transmission Electron Microscopy," *Science Advances* 6 (2020): eaaz7524.

9. C. Drouet, C. Largeot, G. Raimbeaux, and C. Estournès, "Bioceramics: Spark Plasma Sintering (SPS) of Calcium Phosphates," *Advances in Science and Technology* 49 (2006): 45.

10. F. Brouillet, D. Laurencin, D. Grossin, et al., "Biomimetic Apatite-Based Composite Materials Obtained by Spark Plasma Sintering (SPS): Physicochemical and Mechanical Characterizations," *Journal of Materials Science: Materials in Medicine* 26 (2015): 223, https://doi.org/10.1007/s10856-015-5553-9.

11. D. Grossin, S. Rollin-Martinet, C. Estournès, et al., "Biomimetic Apatite Sintered at Very Low Temperature by Spark Plasma Sintering: Physico-chemistry and Microstructure Aspects," *Acta Biomaterialia* 6 (2010): 577–585.

12. A. Indurkar, R. Choudhary, K. Rubenis, and J. Locs, "Advances in Sintering Techniques for Calcium Phosphates Ceramics," *Materials* 14 (2021): 6133.

13. M. Luginina, R. Orru, G. Cao, et al., "First Successful Stabilization of Consolidated Amorphous Calcium Phosphate (ACP) by Cold Sintering: Toward Highly-Resorbable Reactive Bioceramics," *Journal of Materials Chemistry B* 8 (2020): 629–635.

14. K. Rubenis, S. Zemjane, J. Vecstaudza, K. Lazdovica, and J. Bitenieks, "Sintering of Amorphous Calcium Phosphate to Near-Full Density by Uniaxial Compaction at Room Temperature," *Journal of the European Ceramic Society* 42 (2022): 6199–6205, https://doi.org/10.1016/j.jeurceramsoc.2022.06.041.

15. K. Rubenis, S. Zemjane, J. Vecstaudza, J. Bitenieks, and J. Locs, "Densification of Amorphous Calcium Phosphate Using Principles of the Cold Sintering Process," *Journal of the European Ceramic Society* 41 (2021): 912–919.

16. A. Galotta, K. Rubenis, J. Locs, and V. M. Sglavo, "Dissolution-Precipitation Synthesis and Cold Sintering of Mussel Shells-Derived Hydroxyapatite and Hydroxyapatite/Chitosan Composites for Bone Tissue Engineering," *Open Ceramics* 15 (2023): 100418.

17. S. Le Grill, C. Drouet, O. Marsan, et al., "Consolidation of Spray-Dried Amorphous Calcium Phosphate by Ultrafast Compression: Chemical and Structural Overview," *Nanomaterials* 14 (2024): 152.

18. E. Lam, Q. Gu, P. J. Swedlund, S. Marchesseau, and Y. Hemar, "X-Ray Diffraction Investigation of Amorphous Calcium Phosphate and Hydroxyapatite Under Ultra-High Hydrostatic Pressure," *International Journal of Minerals, Metallurgy, and Materials* 22 (2015): 1225–1231.

19. L. Zhang, K. Shi, Y. Wang, et al., "Compression Rate-Dependent Crystallization of Pyridine," *Journal of Physical Chemistry C* 125 (2021): 6983–6989.

20. J. Xu, D. F. Gilson, I. S. Butler, and I. Stangel, "Effect of High External Pressures on the Vibrational Spectra of Biomedical Materials: Calcium Hydroxyapatite and Calcium Fluoroapatite," *Journal of Biomedical Materials Research* 30 (1996): 239–244.

21. L. Mayen, N. D. Jensen, D. Laurencin, et al., "A Soft-Chemistry Approach to the Synthesis of Amorphous Calcium Ortho/Pyrophosphate Biomaterials of Tunable Composition," *Acta Biomaterialia* 103 (2020): 333–345.

22. D. Tuschel, "Raman Thermometry," *Spectroscopy* 31 (2016): 8.

23. P. Colomban and A. Slodczyk, "Raman Intensity: An Important Tool to Study the Structure and Phase Transitions of Amorphous/Crystalline Materials," *Optical Materials* 31 (2009): 1759–1763.

24. C. Koroni, T. Olsen, J. P. Wharry, and H. Xiong, "Irradiation-Induced Amorphous-To-Crystalline Phase Transformations in Ceramic Materials," *Materials* 15 (2022): 5924.

25. S. Le Grill, J. Soulie, Y. Coppel, et al., "Spray-Drying-Derived Amorphous Calcium Phosphate: A Multi-scale Characterization," *Journal of Materials Science* 56 (2021): 1189–1202.

26. M. Alaoui Mansouri, M. Kharbach, and A. Bouklouze, "Current Applications of Multivariate Curve Resolution-Alternating Least Squares (MCR-ALS) in Pharmaceutical Analysis: Review," *Journal of Pharmaceutical Sciences* 113 (2024): 856–865.

27. C. Rey, O. Marsan, C. Combes, C. Drouet, D. Grossin, and S. Sarda, "Characterization of Calcium Phosphates Using

Vibrational Spectroscopies," in *Advances in Calcium Phosphate Biomaterials* (Berlin, Germany: Springer, 2014): 229–266.

28. P. Gras, C. Rey, O. Marsan, S. Sarda, and C. Combes, "Synthesis and Characterisation of Hydrated Calcium Pyrophosphate Phases of Biological Interest," *European Journal of Inorganic Chemistry* 2013 (2013): 5886–5895.

29. W. J. E. M. Habraken, J. Tao, L. J. Brylka, et al., "Ion-Association Complexes Unite Classical and Non-classical Theories for the Biomimetic Nucleation of Calcium Phosphate," *Nature Communications* 4 (2013): 1507.

30. M. Edén, "Structure and Formation of Amorphous Calcium Phosphate and Its Role as Surface Layer of Nanocrystalline Apatite: Implications for Bone Mineralization," *Materialia* 17 (2021): 101107.

31. C.-G. Wang, J.-W. Liao, B.-D. Gou, et al., "Crystallization at Multiple Sites Inside Particles of Amorphous Calcium Phosphate," *Crystal Growth & Design* 9 (2009): 2620.

32. N. Youssef, "A New Percentage of Biphasic Calcium Phosphate (BCP) of Nanoparticles Synthesized Directly by Hydrothermal Process," *Mediterranean Journal of Chemistry* 10 (2020): 355.

33. K. A. Syed, S.-F. Pang, Y. Zhang, G. Zeng, and Y.-H. Zhang, "Micro-Raman Observation on the HPO42–Association Structures in an Individual Dipotassium Hydrogen Phosphate (K2HPO4) Droplet," *Journal of Physical Chemistry A* 116 (2012): 1558–1564.

Supporting Information

Additional supporting information can be found online in the Supporting Information section.